Photoacoustic-ultrasonic dual mode microscopy with local speed-of-sound estimation

Wentian Chen[1], Chao Tao[1,*], Nghia Q. Nguyen[2,3,4], Richard W. Prager[2,3,5], and Xiaojun Liu[1,6]

[1] *MOE Key Laboratory of Modern Acoustics, Department of Physics, Collaborative Innovation Center of Advanced Microstructures, Nanjing University, Nanjing, 210093, China*
[2] *Department of Engineering, University of Cambridge, Cambridge CB2 1PZ, UK*
[3] *Cambridge University – Nanjing Centre of Technology and Innovation, Nanjing, China*
[4] *e-mail: nqn20@cam.ac.uk*
[5] *e-mail: rwp@eng.cam.ac.uk*
[6] *e-mail: liuxiaojun@nju.edu.cn*
[*] *Corresponding author: taochao@nju.edu.cn*

Compiled June 1, 2020

Synthetic aperture imaging and virtual point detection have been exploited to extend the depth-of-view of photoacoustic microscopy. The approach is commonly based on a constant assumed sound speed, which reduces image quality. We propose a new self-adaptive technique to estimate the speed of sound for being integrated with this hybrid strategy. It is accomplished through linear regression between the square of time-of-fight detected at individual virtual detectors and the square of their horizontal distances on the focal plane. The imaging results show our proposed method can significantly improve the lateral resolution, imaging intensity and spatial precision for inhomogeneous tissue.

http://dx.doi.org/10.1364/ao.XX.XXXXXX

Photoacoustic (PA) is a non-invasive imaging technique based on the principles of the photoacoustic effect [1]. In this modality, the image is generated based on illumination from a short-pulse laser. Optical absorbers inside biological tissue absorb laser energy and generate broadband PA (or ultrasonic) signals due to the transient thermoelastic expansion. The signals in time series are acquired by using a spherically focused ultrasound (US) transducer. The distribution of optical absorptions on a scanline along the transducer axis is reconstructed by spatiotemporally mapping the signals back to the imaging domain using the calculated time of flight (TOF). This requires prior information of the speed-of-sound (SOS) in the tissue. A three-dimensional image is obtained by point-by-point scanning the object horizontally (in the x–y plane). The generated image has lateral resolution depending on the center frequency and numerical aperture of the transducer. For a transducer with very high center frequency (from tens to a hundred MHz), the lateral resolution usually ranges from a few tens to hundreds of microns. This modality is known as *photoacoustic microscopy* (PAM) [2] (PAM can be further classified into optical-resolution PAM (OR-PAM) and acoustic-resolution PAM (AR-PAM). In this paper, we are only concerned with AR-PAM, which we refer to as PAM for simplicity). It has wide applications [3–8], particularly in *in vivo* brain imaging [9], microcirculation monitoring [10], cancer detection [11] and flow velocity measurement [12].

A major issue of PAM is that the resolution is only good at the focal depth and is significantly degraded elsewhere [13]. Over the last decade, it has been investigated comprehensively to extend its depth-of-view. Prominent among those studies is the use of the synthetic aperture focusing technique (SAFT) combined with the virtual point detector (VPD) [14]. In this approach, imaging data at individual pixels is generated by combining signals from multiple scans, where the receiving focus of each scan is assumed to be an ideal omnidirectional detector. This assumption is valid within a certain angle. The SAFT+VPD approach helps improve the image resolution and signal-to-noise ratio in out-of-focus regions, and consequently broadens the depth-of-field of the image. SAFT also can be combined with deconvolution in three dimensions and optical fluence compensation to further enhance the spatial resolution [15, 16], and to balance the signal-level distribution over the depth of the imaging region [17].

The quality of PAM, or PA images in general, highly depends on accurate knowledge of the speed of sound. It is related directly to the TOF calculations, used to reconstruct the distribution of optical absorptions on each scanline. In SAFT, TOF is also used to align broadband PA signals extracted from different scans, before superposition. A good prediction of the SOS, however, is difficult to achieve. It changes with temperature and varies up to 10% between different soft biological tissues. Biological tissue that contains both fat and muscle is a typical example. The SOS of muscle is about 1592 m/s [18] while the SOS of fat is about 1440 m/s at the same temperature of 37°C

[19]. If errors in the SOS estimation are too large, there is a loss of coherence among the PA signals which reduces the SNR and degrades image quality [20]. In this study, we investigate a new method to estimate the SOS for SAFT image generation. The proposed method is validated in phantom and *ex vivo* imaging experiments using our PA-US dual-modal microscopy system. The advantage of the new algorithm is demonstrated by comparing its imaging results to those obtained with the prior SOS settings.

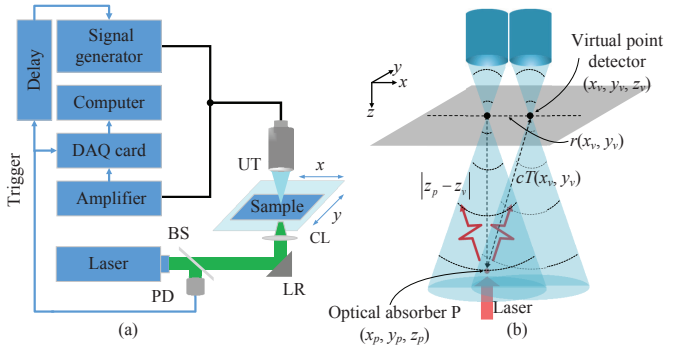

Fig. 1. Block diagram of the dual-mode microscope and illustration of the principle of self-adaptive SOS estimation. (a) Experimental setup of the system, including data acquisition card (DAQ), convex lens (CL), laser reflector (LR), ultrasonic transducer (UT), beamsplitter (BS), and photodiode (PD). (b) Principle of self-adaptive SOS estimation using the virtual detector concept. The transducer is scanning across the x–y plane.

Figure 1 depicts the dual-mode microscope system and the principle of self-adaptive SOS estimation based on VPD. The sample being scanned is alternately illuminated by a laser pulse and an ultrasound beam insonified from a focused transducer. The transducer is then used to receive both PA and backscattered US signals. Thus, two images can be generated simultaneously in the photoacoustic microscopy (PAM) and scanning acoustic microscopy (SAM) modes. Let P be an optical absorber at position $\mathbf{x}_p = (x_p, y_p, z_p)$. In SAFT, data at P is generated by compounding signals received at multiple VPDs (x_v, y_v, z_v) on the focal plane $z = z_v$. From Fig. 1(b), one can establish a relationship between the SOS, c and the TOF, $T(x_v, y_v)$ extracted from the ultrasonic waveform received at (x_v, y_v, z_v), given by

$$r^2(x_v, y_v) = c^2 T^2(x_v, y_v) - (z_p - z_v)^2 \ , \qquad (1)$$

where $r(x_v, y_v) = \left((x_p - x_v)^2 + (y_p - y_v)^2\right)^{1/2}$ and $|z_p - z_v|$ are the horizontal and vertical distances between P and the VPD located at (x_v, y_v, z_v). If T and r can be determined for each pair of the detected PA signals and the corresponding VPD positions with respect to a specific absorber, sound-speed c corresponding to the absorber can be estimated by linear regression between r^2 and T^2 using the least square criterion.

In practice, it is difficult to measure $T = T(x_v, y_v)$ directly. Instead, we estimate it through the time difference $\Delta T(x_v, y_v)$ from the first arrival time detected at the perpendicular VPD (x_p, y_p, z_v). Thus, $T(x_v, y_v)$ is given by

$$T(x_v, y_v) = T(x_p, y_p) + \Delta T(x_v, y_v) \ , \qquad (2)$$

where $T(x_p, y_p)$ is the first arrival time at VPD (x_p, y_p, z_v). The time delay is estimated by maximizing the cross-correlation

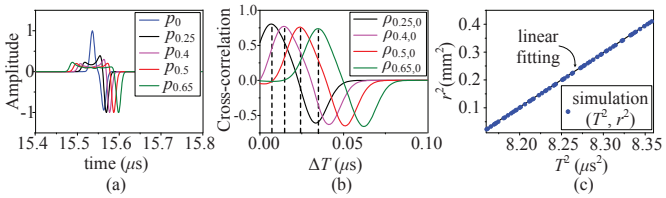

Fig. 2. A simulation for the self-adaptive estimation of the SOS. (a) PA signals p_r generated from an absorber at depth 23 mm and detected by the VPD at horizontal distances r, including $r = 0$ mm, 0.25 mm, 0.4 mm, 0.5 mm, and 0.65 mm. Each curve is obtained by normalizing its maximum amplitude. (b) The cross-correlation $\rho_{r,0}$ between PA signals p_r and p_0 plotted in (a), from which ΔT is drawn based on the peaks of the cross-correlation curves. And (c) linear fitting between r^2 and T^2 calculated in Eq. (3).

between the two received signals, that is

$$\Delta T(x_v, y_v) = \underset{\Delta t}{\operatorname{argmax}}\, \rho\left[p_{x_v,y_v}(t - \Delta t)\, p_{x_p,y_p}(t)\right] \ , \qquad (3)$$

where $p_{x_v,y_v}(t)$ and $p_{x_p,y_p}(t)$ are the ultrasonic waveforms obtained at VPDs (x_v, y_v, z_v) and (x_p, y_p, z_v), respectively, $\rho[\cdot]$ is the cross-correlation between the two waveforms. To improve the SNR, $p_{x_v,y_v}(t)$ is replaced by the superposition of all waveforms received at VPDs having the same horizontal distance $r(x_v, y_v)$. From all pairs of (T^2, r^2), the SOS for imaging pixel P can be estimated.

The estimated SOS is combined to generate focusing signals. Similar to [14], we also combine the signal generation with a coherent factor (CF) for enhancing the lateral resolution and suppressing sidelobes, given by

$$\mathrm{CF}(\mathbf{x}_p) = \frac{\left|\sum_{x_v,y_v}^{x'^2+y'^2\le R^2} p_{x_v,y_v}\left(\frac{\kappa z_v}{\hat{c}_p} - \beta\kappa\tau_{x',y',z'}\right)\right|^2}{N\sum_{x_v,y_v}^{x'^2+y'^2\le R^2}\left|p_{x_v,y_v}\left(\frac{\kappa z_v}{\hat{c}_p} - \beta\kappa\tau_{x',y',z'}\right)\right|^2} \ , \qquad (4)$$

where N is the total number of superimposed signals at imaging point P. Thus, the imaging pixel intensity at P is calculated as

$$A(\mathbf{x}_p) = \mathcal{H}\left[\sum_{x_v,y_v}^{x'^2+y'^2\le R^2} \mathrm{CF}(\mathbf{x}_p)\, p_{x_v,y_v}\left(\frac{\kappa z_v}{\hat{c}_p} - \beta\kappa\tau_{x',y',z'}\right)\right] \ , \qquad (5)$$

where $\mathcal{H}[\cdot]$ represents the Hilbert transform, $x' = x_p - x_v$, $y' = y_p - y_v$, $z' = z_p - z_v$, and $\tau_{x',y',z'} = \left[|z'| - \left(x'^2 + y'^2 + z'^2\right)^{1/2}\right]/\hat{c}_p$, where $\hat{c}_p$ is the SOS estimated from the linear regression at P. R is the radius of the synthetic aperture in horizontal view, $\beta = 1$ for $z' > 0$ and $\beta = -1$ otherwise, $\kappa = 1$ for generating PAM image. The SAM image is generated using the same expression with $\kappa = 2$.

We first validate our estimation method using simulation, as shown in Fig. 2. The signals are simulated for a focused transducer with a central frequency 30 MHz and a focal length of 19 mm.The scanning step is 50 μm. Four spherical optical absorbers are distributed evenly at depths from 19 mm to 25 mm. The SOS is varied from 1300 m/s to 1700 m/s in the vertical direction. Figure 2(a) plots the ultrasonic waves emitted from an absorber at depth 23 mm, and received at VPDs located at five horizontal distances, $r = 0$ mm, 0.25 mm, 0.4 mm, 0.5 mm, and 0.65 mm. The cross-correlations among these waveforms are plotted in Fig. 2(b), from which the time delays between them are estimated. The relationship between horizontal distance r^2

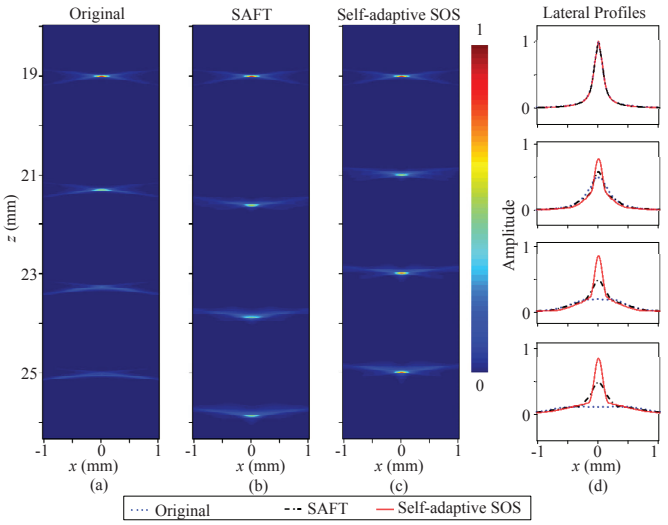

Fig. 3. Simulated images of four optical absorbers at different depths obtained with different strategies, including (a) Original PAM generated with a fix SOS of 1500 m/s, (b) SAFT image with a fixed SOS of 1700 m/s, (c) and SAFT image with self-adaptive SOS. The images are normalized by the peak of intensities. Lateral profiles of the four optical absorbers obtained with these strategies are plotted in (d). The legend at the bottom of the figure applies to the four lateral profiles.

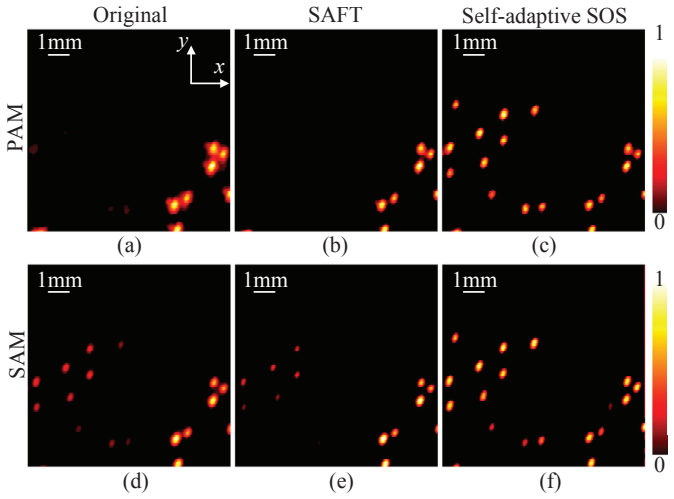

Fig. 4. Images of black polymer microspheres generated with PA signals (PAM) and US signals (SAM) using different approaches to image reconstruction. Figures (a) and (d) show the original images with an assumed SOS of 1500 m/s. Figures (b) and (e) shows the results using the same SOS with the SAFT method, while those obtained with SAFT and our adaptive SOS are showed in (c) and (f). Each image is normalized by the intensity peak of the same row.

and the corresponding TOFs T^2 for the absorber at 23 mm are depicted in Fig. 2(c). Using linear regression, we can estimate the SOS at the absorber, $\hat{c} \approx 1401.2$ m/s, which is very close to its true average value of 1400 m/s.

Figure 3 show the images of the same absorbers simulated with different strategies, including (a) the original with a fixed SOS of 1500 m/s, (b) SAFT with a fixed SOS of 1700 m/s, and (c) SAFT combined with our self-adaptive approach to estimate the SOS. In the figure, it is shown clearly that the SAFT image in (b) helps enhance the image intensity significantly compared to the original. However, the absorbers' locations are shifted because of the inaccurate SOS. By combining this with our self-adaptive SOS, we are able to position these absorbers correctly. This also shows highly focused resolution for absorbers far from the focal depth. To observe the enhancement more clearly, we plot the lateral profiles for each of the absorbers in Fig. 3(d). In the plot, the self-adaptive SOS has the best resolution both in terms of image intensity and the width of the mainlobe. Take an absorber at 25 mm (6 mm away from the focus) as an example. Compared to the original PAM, the SAFT and self-adaptive SOS can increase the peak value of the lateral profile to two-fold and four-fold, respectively. At the same time, they help reduce the full width at half maximum (FWHM) to three-fold and five-fold compared to that of PAM.

Next we evaluate our method on datasets obtained from a phantom and *ex vivo* brain imaging studies. In both experiments, the PA signals are excited by a Nd:YAG laser (EXPL-532-2Y, Spectra-Physics Inc.) with a wavelength of 532 nm, a repetition rate of 10 kHz, and a pulse duration of 8 ns. The SAM image is generated by a pulse generator (CTS-8077PR, Goworld Corp.). The spherically focused US transducer (V375-SU, Olympus Corp.) has a central frequency of 30 MHz focused at 19 mm. It is 6.3 mm in diameter and has a −6 dB bandwidth of 78.27%. Acoustic coupling is achieved through water. The detected PA/US signals are amplified by a low noise amplifier (CTS-8077PR, Goworld Corp.) with a gain of 46 dB and digitized by a data acquisition card (NI-5761, NI Corp.) at a sampling frequency of 250 MHz. A photodiode (PDA 10A-EC, Thorlabs Inc.) is used to monitor the intensity of the laser pulse. Its output is also used as a time reference to trigger the data acquisition card and control the pulse generator. The sample is scanned with a step size of 50 μm under the control of a two-dimensional motorized translational stage, which allows us to obtain three-dimensional images.

A phantom with a thickness of 2 mm approximately was made from agar, 1-propanol, and water. Black polymer microspheres of about 200 μm in diameter were randomly suspended in the top and bottom surfaces of the phantom.The scanning range is 8×8 mm. The SOS estimated in the right part of the phantom is about 1497 m/s at 25°C while that in the left is raised to about 1588 m/s by adding 1-propanol [20]. Figure 4 shows the AR-PAM and SAM images of the bottom surface generated with different methods. The surface is about 2 mm away from the focus. The PAM and SAM images generated with a fixed focus and a pre-set SOS of 1500 m/s are shown in (a) and (d), while those generated with SAFT using the same SOS are shown (b) and (e) respectively. Compared to the images with a fixed focus, the SAFT images show the spheres with better resolution. However, the spheres on the left side are not visible on these images because of the inaccurate SOS. In image (e), the lower intensities of the absorbers on the left, compared to those in (d), is explained by the normalization on a higher intensity peak of the absorbers on the right generated with a more accurate SOS for this region. Meanwhile, the images obtained with the SAFT combined with our self-adaptive SOS are showed in (c) and (f). They have visible spheres on the left side with equal quality to those showed on the right side of the SAFT images.

Finally, we demonstrate the method in an *ex vivo* imaging experiment of a mouse brain. The imaging results are shown in Fig. 5. The scanning range is 15×10 mm. Images obtained with a fixed focus transducer and a SOS of 1500 m/s are shown in the first column while those obtained with SAFT strategy using prior SOS 1300 m/s are shown in the second column and results

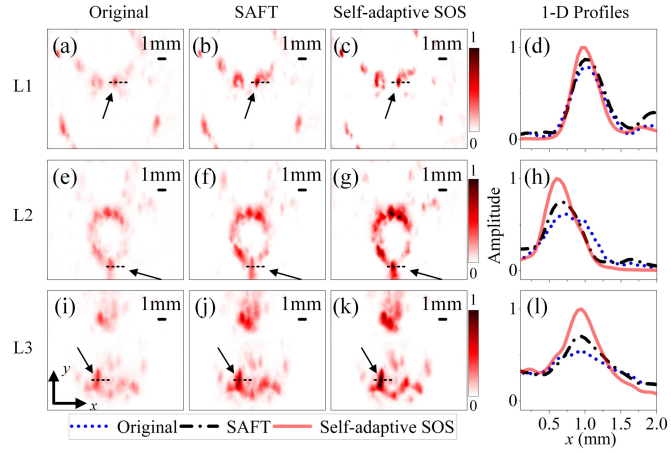

Fig. 5. PAM images for different layers (L_1, L_2, and L_3) of the mouse brain. The original images are shown in (a), (e) and (i) (*first column*), while those obtained with the SAFT method are shown in (b), (f) and (j) (*second column*) and the results of self-adaptive SOS are shown in (c), (g) and (k) (*third column*). Each image is normalized by the intensity peak of the same row.1-D profiles on the black dotted lines obtained with the three strategies of the three different layers are shown in (d), (h), (l) (*fourth column*). The legend at the bottom of the figure applies to the three lateral profiles.

obtained with SAFT using the self-adaptive SOS approach are shown in the third column. Each column has three images corresponding to three layers at different depths ((L_1, L_2, and L_3)). The distance between each layer is 1.5 mm, and L_1 is about 1 mm below the focus. Results show that the patterns in the mouse brain on all the layers are reconstructed with clearer shapes and much higher intensities with the SAFT and self-adaptive SOS. This confirms the advantages of the proposed method, including benefits to image resolution, spatial accuracy, and image contrast. In order to show the enhancement more clearly, we plot the 1-D profiles on the black dotted lines for each layer in Fig. 5(d), (h), (l). Compared to simulation, the improvements on image quality offered by the SAFT and self-adaptive SOS are reduced. Taking the 1-D profiles of L_3 as an example. Compared to the original PAM, the SAFT and self-adaptive SOS can increase the peak value of the lateral profile by 29.3% and 83.7% while the full width at half maximum (FWHM) are reduced to 60.7% and 42.9% of that of PAM. The less improvements of the self-adaptive SOS could come from some internal noise inside our imaging system and uncertainty factors in *ex vivo* experiments.

In summary, we propose a new method of estimating the speed-of-sound in photoacoustic-ultrasound dual-mode microscopy. The method is based on a synthetic aperture imaging technique, combined with the concept of a virtual point detector. By demonstrating the new approach through a series of experiments, including simulation, phantom and *ex vivo* studies, we have shown that the proposed method effectively improves the lateral resolution, depth-of-field, imaging intensity and spatial precision for inhomogeneous tissues. Implementing the proposed method on data from *in vivo* studies remains for further investigation. Since biological tissue has a sound-speed that varies by as much as 10%, the proposed method may have wide potential applications in practical biomedical imaging.

Acknowledgements. This work was supported by the National Natural Science Foundation of China (11834008 and 11874217).

Disclosures. The authors declare no conflicts of interest.

REFERENCES

1. L. V. Wang and S. Hu, Science **335**, 1458 (2012).
2. H. F. Zhang, K. Maslov, G. Stoica, and L. V. Wang, Nat. Biotechnol. **24**, 848 (2006).
3. Z. Guo, Y. Li, and S.-L. Chen, Opt. Lett. **43**, 1119 (2018).
4. J. Park, S. Jeon, J. Meng, L. Song, J. S. Lee, and C. Kim, J. Biomed. Opt. **21**, 036010 (2016).
5. J. Brunker and P. Beard, Biomed. Opt. Express. **7**, 2789 (2016).
6. X. Gao, C. Tao, X. Wang, and X. Liu, Opt. Lett. **40**, 970 (2015).
7. M. S. Singh and H. Jiang, Opt. Lett. **39**, 3970 (2014).
8. X. Yang, Y. Zhang, K. Zhao, Y. Zhao, Y. Liu, H. Gong, Q. Luo, and D. Zhu, IEEE Trans. Med. Imaging. **35**, 1903 (2016).
9. M. Kneipp, J. Turner, H. Estrada, J. Rebling, S. Shoham, and D. Razansky, J. Biophotonics **57**, 117 (2016).
10. Y. Tsunoi, K. Yoshimi, R. Watanabe, N. Kumai, M. Terakawa, and S. Sato, Jpn. J. Appl. Phys. **57**, 127001 (2018).
11. X. Leng, J. William Chapman, B. Rao, S. Nandy, R. Chen, R. Rais, I. Gonzalez, Q. Zhou, D. Chatterjee, M. Mutch, and Q. Zhu, Biomed. Opt. Express. **9**, 5159 (2018).
12. J. Brunker and P. Beard, Sci. Rep. **6**, 20902 (2016).
13. S. Jeon, J. Kim, D. Lee, J. W. Baik, and C. Kim, Photoacoustics. **15**, 100141 (2019).
14. M.-L. Li, H. F. Zhang, K. Maslov, G. Stoica, and L. V. Wang, Opt. Lett. **31**, 474 (2006).
15. D. Cai, Z. Li, Y. Li, Z. Guo, and S.-L. Chen, Opt. Express **25**, 057001 (2017).
16. D. Cai, Z. Li, and S.-L. Chen, Biomed. Opt. Express. **7**, 369 (2016).
17. V. V. Perekatova, M. Y. Kirillin, I. V. Turchin, and P. V. Subochev, J. Biomed. Opt. **23**, 091414 (2018).
18. R. L. Marsh, J. Biomech. **49**, 4138 (2016).
19. R. Ortega, L. Leija, and A. Vera, 2009 Pan Am. Heal. Care Exch. pp. 58–61 (2009).
20. Q. Ding, C. Tao, and X. Liu, Opt. Express **6**, 6141 (2017).

FULL REFERENCES

1. L. V. Wang and S. Hu, "Photoacoustic tomography: In vivo imaging from organelles to organs," Science **335**, 1458–1462 (2012).
2. H. F. Zhang, K. Maslov, G. Stoica, and L. V. Wang, "Functional photoacoustic microscopy for high-resolution and noninvasive in vivo imaging," Nat. Biotechnol. **24**, 848–851 (2006).
3. Z. Guo, Y. Li, and S.-L. Chen, "Miniature probe for in vivo optical and acoustic-resolution photoacoustic microscopy," Opt. Lett. **43**, 1119–1122 (2018).
4. J. Park, S. Jeon, J. Meng, L. Song, J. S. Lee, and C. Kim, "Delay-multiply-and-sum-based synthetic aperture focusing in photoacoustic microscopy," J. Biomed. Opt. **21**, 036010–1–10 (2016).
5. J. Brunker and P. Beard, "Velocity measurements in whole blood using acoustic resolution photoacoustic doppler," Biomed. Opt. Express. **7**, 2789–2806 (2016).
6. X. Gao, C. Tao, X. Wang, and X. Liu, "Quantitative imaging of microvasculature in deep tissue with a spectrum-based photoacoustic microscopy," Opt. Lett. **40**, 970–973 (2015).
7. M. S. Singh and H. Jiang, "Elastic property attributes to photoacoustic signals: an experimental phantom study," Opt. Lett. **39**, 3970–3973 (2014).
8. X. Yang, Y. Zhang, K. Zhao, Y. Zhao, Y. Liu, H. Gong, Q. Luo, and D. Zhu, "Skull optical clearing solution for enhancing ultrasonic and photoacoustic imaging," IEEE Trans. Med. Imaging. **35**, 1903–1906 (2016).
9. M. Kneipp, J. Turner, H. Estrada, J. Rebling, S. Shoham, and D. Razansky, "Effects of the murine skull in optoacoustic brain microscopy," J. Biophotonics **57**, 117–123 (2016).
10. Y. Tsunoi, K. Yoshimi, R. Watanabe, N. Kumai, M. Terakawa, and S. Sato, "Quality improvement of acoustic-resolution photoacoustic imaging of skin vasculature based on practical synthetic-aperture focusing and bandpass filtering," Jpn. J. Appl. Phys. **57**, 127001–1–6 (2018).
11. X. Leng, J. William Chapman, B. Rao, S. Nandy, R. Chen, R. Rais, I. Gonzalez, Q. Zhou, D. Chatterjee, M. Mutch, and Q. Zhu, "Feasibility of co-registered ultrasound and acoustic-resolution photoacoustic imaging of human colorectal cancer," Biomed. Opt. Express. **9**, 5159–5172 (2018).
12. J. Brunker and P. Beard, "Acoustic resolution photoacoustic doppler velocimetry in blood-mimicking fluids," Sci. Rep. **6**, 20902–1–16 (2016).
13. S. Jeon, J. Kim, D. Lee, J. W. Baik, and C. Kim, "Review on practical photoacoustic microscopy," Photoacoustics. **15**, 100141–1–16 (2019).
14. M.-L. Li, H. F. Zhang, K. Maslov, G. Stoica, and L. V. Wang, "Improved in vivo photoacoustic microscopy based on a virtual-detector concept," Opt. Lett. **31**, 474–476 (2006).
15. D. Cai, Z. Li, Y. Li, Z. Guo, and S.-L. Chen, "Photoacoustic microscopy in vivo using synthetic-aperture focusing technique combined with three-dimensional deconvolution," Opt. Express **25**, 057001–1–5 (2017).
16. D. Cai, Z. Li, and S.-L. Chen, "In vivo deconvolution acoustic-resolution photoacoustic microscopy in three dimensions," Biomed. Opt. Express. **7**, 369–380 (2016).
17. V. V. Perekatova, M. Y. Kirillin, I. V. Turchin, and P. V. Subochev, "Combination of virtual point detector concept and fluence compensation in acoustic resolution photoacoustic microscopy," J. Biomed. Opt. **23**, 091414–1–11 (2018).
18. R. L. Marsh, "Speed of sound in muscle for use in sonomicrometry," J. Biomech. **49**, 4138–4141 (2016).
19. R. Ortega, L. Leija, and A. Vera, "Measurement of ultrasonic properties of fat biological phantom," 2009 Pan Am. Heal. Care Exch. pp. 58–61 (2009).
20. Q. Ding, C. Tao, and X. Liu, "Photoacoustics and speed-of-sound dual mode imaging with a long depth-of-field by using annular ultrasound array," Opt. Express **6**, 6141–6150 (2017).